APPLIED PHYSICS

High-frequency cavity optomechanics using bulk acoustic phonons

Prashanta Kharel[1]*, Glen I. Harris[2], Eric A. Kittlaus[1], William H. Renninger[1], Nils T. Otterstrom[1], Jack G. E. Harris[2], Peter T. Rakich[1]*

To date, microscale and nanoscale optomechanical systems have enabled many proof-of-principle quantum operations through access to high-frequency (gigahertz) phonon modes that are readily cooled to their thermal ground state. However, minuscule amounts of absorbed light produce excessive heating that can jeopardize robust ground-state operation within these microstructures. In contrast, we demonstrate an alternative strategy for accessing high-frequency (13 GHz) phonons within macroscopic systems (centimeter scale) using phase-matched Brillouin interactions between two distinct optical cavity modes. Counterintuitively, we show that these macroscopic systems, with motional masses that are 1 million to 100 million times larger than those of microscale counterparts, offer a complementary path toward robust ground-state operation. We perform both optomechanically induced amplification/transparency measurements and demonstrate parametric instability of bulk phonon modes. This is an important step toward using these beam splitter and two-mode squeezing interactions within bulk acoustic systems for applications ranging from quantum memories and microwave-to-optical conversion to high-power laser oscillators.

INTRODUCTION

The coherent control of mechanical objects (*1*–*4*) can enable applications ranging from sensitive metrology (*5*) to quantum information processing (*6*, *7*). An array of devices (*8*–*14*) ranging from nano-optomechanical crystals to suspended micromirrors have been used to manipulate mechanical degrees of freedom using light. Central to the field of cavity optomechanics—and more generally to quantum information science—is the ability to harness long-lived mechanical excitations at high frequencies (*15*). Long-lived high-frequency phonons can be initialized deep in their quantum ground states and can preserve coherent information for extended periods of time in the presence of various decoherence channels. Optomechanical systems using high-frequency (gigahertz) phonons have enabled ground-state cooling (*16*), quantum control at the single-phonon level (*17*, *18*), and remote entanglement between mechanical resonators (*19*–*21*). However, it may be difficult to implement more sophisticated quantum protocols using these systems because of spurious forms of laser heating that threaten robust ground-state operation within microscale and nanoscale systems (*16*, *18*, *22*). New device strategies may be necessary to mitigate these decoherence mechanisms for robust quantum optical control of high-frequency phonons.

Efficient optomechanical coupling to high-frequency bulk acoustic waves within macroscopic systems offers an alternative path to robust quantum control of phonons. Optical access to these phonons within pristine crystalline solids yield greatly reduced surface interactions and favorable thermal characteristics to mitigate spurious laser heating (*23*, *24*). These resonators also grant access to world-record $f \cdot Q$ products (*23*), a key figure of merit that characterizes decoupling of a resonator from its thermal environment (*15*). While these bulk acoustic phonon modes have been accessed through Brillouin-like coupling using a free-space laser beam (*24*, *25*), new strategies are needed to translate this physics into cavity optomechanical systems as the basis for phonon counting (*17*, *26*), generation of nonclassical mechanical states (*18*), and efficient transduction of information between optical and phononic domains (*27*).

Here, we realize a cavity-optomechanical system that harnesses high-frequency (13 GHz) bulk acoustic phonon modes within a macroscopic crystal, offering an array of properties that open the door to robust quantum manipulation of phonons. These high-frequency phonons, with large (20 μg) motional masses, are used to mediate resonant coupling between two distinct modes of an optical cavity through Brillouin interactions. To enable beam splitter and entanglement interactions as the basis for quantum optical control of phonons, we engineer the multimode spectrum of the optical cavity to break the symmetry between the Stokes and anti-Stokes processes while allowing resonant driving of a chosen optical mode. Resonant driving allows us to attain intracavity photon numbers that are more than six orders of magnitude larger than those of high-frequency microscale counterparts (*16*). These resonantly enhanced photon numbers permit large (megahertz) optomechanical coupling rates and greater than unity cooperativities, necessary for efficient control of phonons using light. In addition, we demonstrate that phase-matched Brillouin interactions produce controllable coupling to one or more phonon modes, opening the door to new forms of multimode entanglement (*28*). Looking beyond the field of cavity quantum optomechanics, this device strategy presents new opportunities for sensitive materials spectroscopy and oscillator technologies.

Bulk crystalline optomechanical system

In what follows, we explore optomechanical interactions mediated by macroscopic phonon modes within the bulk crystalline cavity optomechanical system of Fig. 1A. A 5.2-mm-thick flat-flat quartz crystal is placed within a nearly hemispherical Fabry-Pérot cavity having high-reflectivity (98%) mirrors; this optomechanical assembly is cooled to ~8 K temperatures to greatly extend the phonon lifetimes within crystalline quartz. At room temperature, high-frequency phonons (>10 GHz) have a mean free path (~100 μm) that is much smaller than the crystal dimension. Just as the optical Fabry-Pérot resonator supports a series of standing electromagnetic waves (red and

[1]Department of Applied Physics, Yale University, New Haven, CT 06511, USA. [2]Department of Physics, Yale University, New Haven, CT 06520, USA.
*Corresponding author. Email: prashanta.kharel@yale.edu (P.K.); peter.rakich@yale.edu (P.T.R.)

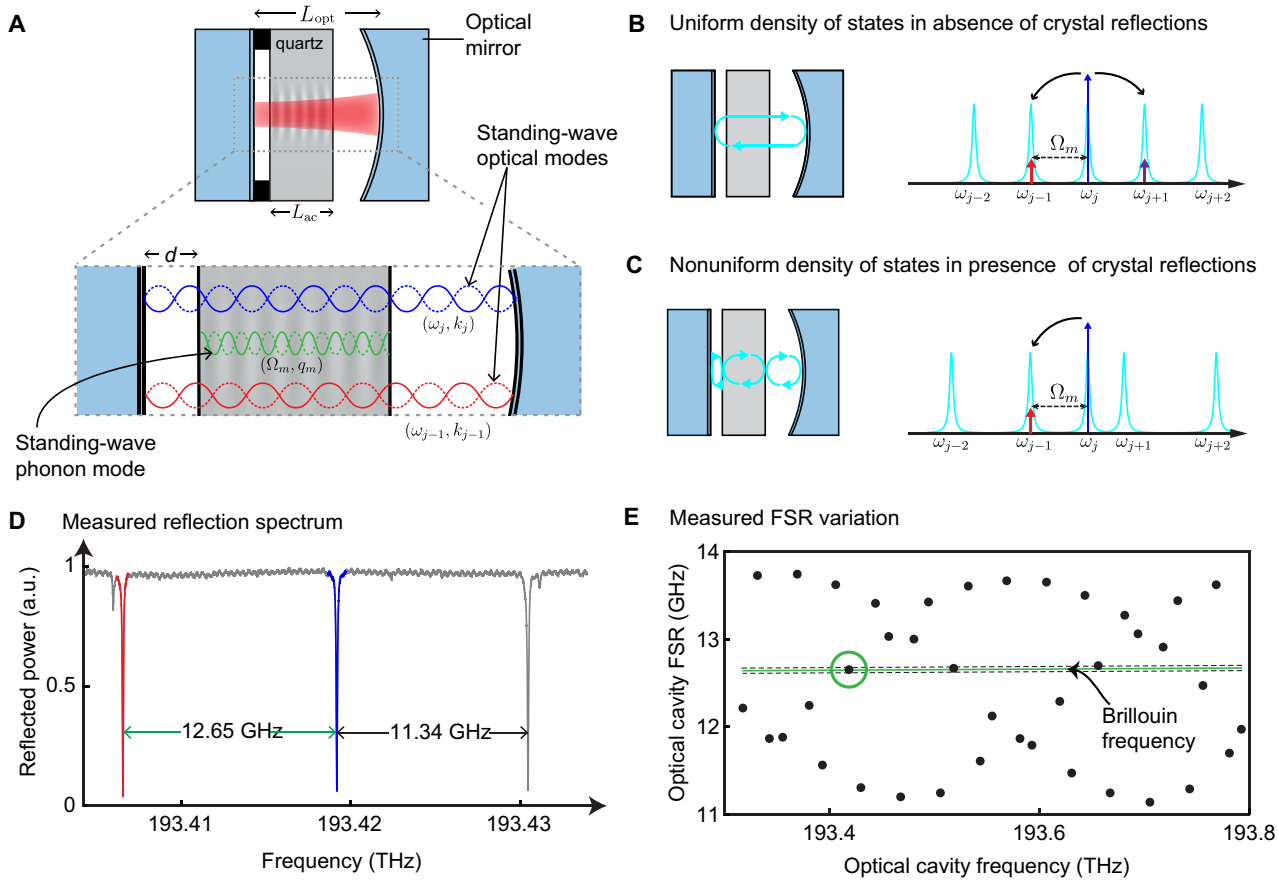

Fig. 1. The multimode cavity optomechanical system. (**A**) Schematic of an optomechanical system that consists of a bulk acoustic wave resonator that is placed inside an optical cavity. Two distinct standing-wave longitudinal optical modes interact through electrostrictive coupling with a standing-wave longitudinal phonon mode formed within the planar crystalline quartz crystal at cryogenic temperatures (~8 K). Large mode volumes for both light and sound result from macroscopic geometrical parameters: $L_{ac} \simeq 5.2$ mm, $L_{opt} \simeq 9.1$ mm, and $d \simeq 0.15$ mm. (**B**) Assuming no optical reflections in the quartz-vacuum interface, one obtains equally spaced longitudinal optical modes. Therefore, a phonon mode mediating intermodal optomechanical interactions can scatter incident laser light at ω_j to adjacent optical modes ω_{j+1} and ω_{j-1} with nearly equal scattering rates. (**C**) However, modest optical reflections (~4%) in the quartz-vacuum interface, which lead to notable nonuniformity in optical mode spacing, can be exploited to bias our system to strongly favor one scattering process ($\omega_j \rightarrow \omega_{j-1}$) over the other ($\omega_j \rightarrow \omega_{j+1}$). The variation in cavity resonances arises because of dispersive shifts of cavity resonances arising from multipath interference. (**D**) The reflection spectrum of the optical cavity obtained by frequency sweeping an incident laser light reveals this variation in optical mode spacing (or FSR) between adjacent fundamental Gaussian modes. a.u., arbitrary units. (**E**) Measurement of the FSR over a wider frequency range by sweeping the laser from 1548- to 1552-nm wavelength shows large undulation (2.6 GHz) in the FSR as a function of the optical cavity frequency. Consequently, we find multiple pairs of resonances with frequency differences that are equal to the Brillouin frequency, which is a necessary requirement for intermodal optomechanical coupling in our system.

blue) seen in Fig. 1A, the planar surfaces of the quartz crystal produce acoustic reflections to form an acoustic Fabry-Pérot resonator that supports a series of standing-wave elastic modes (green) at these low temperatures. To avoid anchoring losses, an annular spacer prevents the crystal surface from contacting the mirror; this same spacer sets the position of the crystal (d) within the cavity.

These high-frequency bulk acoustic phonon modes are used to mediate efficient coupling between distinct longitudinal optical modes of the Fabry-Pérot cavity through a multiresonant (or multimode) optomechanical process. Coupling occurs through a Brillouin-like optomechanical process when the time-modulated electrostrictive optical force distribution, produced by the interference between distinct modes of the Fabry-Pérot cavity, matches the elastic profile (and frequency) of a bulk acoustic phonon mode. The same intrinsic photoelastic response that generates the optical forces within the crystal also modulates the refractive index of the crystal via elastic-wave motion. Through the formation of a time-modulated photoelastic grating, these "Brillouin-active" elastic waves mediate dynamical Bragg scattering (or energy transfer) between distinct longitudinal modes of the optical Fabry-Pérot cavity.

Because of the extended nature of the optomechanical interaction within the crystal, phase matching and energy conservation determine the set of phonon modes (Ω_m, q_m) that can mediate resonant coupling between adjacent optical modes (ω_j, k_j) and (ω_{j-1}, k_{j-1}) of the Fabry-Pérot cavity (see Fig. 1A). One finds that the Brillouin-active phonons must satisfy the conditions $q_m = k_{j-1} + k_j$ and $\Omega_m = \omega_j - \omega_{j-1}$ to mediate dynamical Bragg scattering within the crystal. Neglecting some details pertaining to modal overlaps, one expects that phonons in a narrow band of frequencies near the Brillouin frequency ($\Omega_B \simeq 2\omega_j \upsilon_a / \upsilon_o$) can meet this condition; here, $\upsilon_a(\upsilon_o)$ is the speed of sound (light) in the quartz crystal. Within the z-cut crystalline quartz substrate, this expression leads us to expect intermodal coupling at $\Omega_B \simeq 2\pi \times 12.7$ GHz when driving the optical cavity with 1.55-μm wavelength light. On the basis of the resonance condition,

we seek a Fabry-Pérot design whose free spectral range (FSR), defined as $\omega_{\mathrm{FSR}}^{j} = \omega_j - \omega_{j-1}$, matches the Brillouin frequency Ω_B.

Most applications of optomechanical interactions require a means of selecting between the Stokes and anti-Stokes interactions. Conventional single-mode cavity optomechanical systems use the detuning of an external drive field from a single-cavity resonance to produce this asymmetry. By comparison, this multimode system offers the possibility for resonant pumping, which carries many advantages (see Discussion). However, in the case when the optical Fabry-Pérot resonator has regular mode spacing (i.e., $\omega_{\mathrm{FSR}}^{j} = \omega_{\mathrm{FSR}}^{j-1}$), resonant driving of the optical cavity presents a problem; a Brillouin-active phonon mode (Ω_m) that matches the multimode resonant condition will resonantly scatter incident photons of frequency ω_j to adjacent cavity modes ω_{j-1} and ω_{j+1} with nearly equal probabilities (see Fig. 1B).

The introduction of the quartz crystal into the optical Fabry-Pérot resonator provides an elegant means of solving this problem; modest optical reflections (~4%) produced by the surfaces of the crystal shift the modes of the Fabry-Pérot cavity. As a result, the typically uniform density of modes (Fig. 1B) is transformed into a highly nonuniform density of modes (Fig. 1C) such that $\omega_{\mathrm{FSR}}^{j} \neq \omega_{\mathrm{FSR}}^{j-1}$. Using this strategy, we are able to choose between the Stokes ($\omega_j \rightarrow \omega_{j-1}$) and anti-Stokes ($\omega_{j-1} \rightarrow \omega_j$) processes with high selectivity, even when the external drive field is directly on resonance. For example, Fig. 1C illustrates how a dispersively engineered mode spacing ($\omega_{\mathrm{FSR}}^{j} \neq \omega_{\mathrm{FSR}}^{j-1}$) permits us to bias the system for Stokes scattering with resonant optical driving at frequency ω_j.

This modification to the density of modes can be seen from reflection measurements of this bulk crystalline optomechanical system (Fig. 1D), which reveal a large (~21%) undulation in the FSR of the optical Fabry-Pérot resonator; Fig. 1E shows the measured frequency spacing between adjacent optical resonances ($\omega_{\mathrm{FSR}}^{j} = \omega_{j+1} - \omega_j$) when an incident laser field is mode-matched to the fundamental Gaussian mode of the cavity. The observed variation in optical FSR agrees well with scattering matrix treatments of the system (see section S1). The large spread in mode separations makes it straightforward to find pairs of optical modes whose frequency difference satisfies the multimode resonance condition. Within the measurements of Fig. 1E, one can readily identify three sets of modes (green) that satisfy this condition. Moreover, this dispersive shift permits us to fine-tune the FSR of a given mode pair to match Brillouin frequency through a small (<1 K) change in temperature (see section S1).

Even with resonant driving of the optical mode, this form of symmetry breaking results in a large (>1000-fold) difference between the Stokes and anti-Stokes scattering rates. In conventional single-mode cavity optomechanical systems, this large Stokes/anti-Stokes asymmetry is produced by far-detuning the drive from an optical cavity at the expense of the intracavity photon number. In contrast, this multimode optomechanical system permits greatly enhanced intracavity photon numbers for the same input power through resonant driving (*29*). The relative strength of the Stokes/anti-Stokes scattering rates in the case of resonant driving is determined by the ratio $(2\Delta\omega/\kappa)^2$, where $\Delta\omega = \omega_{\mathrm{FSR}}^{j+1} - \omega_{\mathrm{FSR}}^{j}$ is the difference in the FSR between adjacent optical modes and κ is the optical mode linewidth (see section S7). Because $\Delta\omega$ is well resolved from the linewidth (i.e., $2\Delta\omega/\kappa \simeq 36$), we can virtually eliminate the Stokes or anti-Stokes interaction by resonantly exciting an appropriately chosen mode.

The multimode coupling described above can be represented by the interaction Hamiltonian $H_{\mathrm{int}}^{m} = -\hbar g_0^m \left(a_{j+1}^{\dagger} a_j b_m + a_j^{\dagger} a_{j+1} b_m^{\dagger}\right)$ (*30*). Here, $a_j^{\dagger}$ is the creation operator for the optical mode at frequency ω_j, $b_m^{\dagger}$ is the creation operator for the phonon mode at frequency Ω_m, and g_0^m is the single-photon coupling rate that characterizes the strength of the optomechanical interaction (see section S2, A to C). This single-photon coupling rate describes the change in the frequency spacing between the two optical modes resulting from the dynamical modulation of the refractive index of the crystal. Because the acoustic FSR ($\upsilon_a/2L_{\mathrm{ac}}$) of the bulk acoustic waves within our quartz substrate is much smaller than the optical linewidth ($\kappa/2\pi$), more than one phonon mode (Ω_m) near the Brillouin frequency (Ω_B) can participate in the optomechanical coupling. Hence, the total interaction Hamiltonian, which includes contributions from all these phonon modes, becomes $H_{\mathrm{int}} = \sum_m H_{\mathrm{int}}^{m}$.

To calculate the single-photon coupling rate, g_0^m, we consider the interaction energy $H^{\mathrm{int}} = -\int_v dV \sigma(\mathbf{r}) \cdot S(\mathbf{r})$ for photoelasticity-mediated coupling between light and sound fields, where $\sigma(\mathbf{r})$ is the electrostrictively induced stress and $S(\mathbf{r})$ is the phonon mode's strain field. For simplicity, we assume coupling between longitudinal phonon modes propagating in the z direction with linearly polarized electromagnetic modes in the x direction. The dominant stress tensor component $\sigma \equiv \sigma_z = -(1/2)\epsilon_0 \epsilon_r^2 p_{13} E_x(z)^2$, where ϵ_0 (ϵ_r) is the vacuum (relative) permittivity of the optical cavity, p_{13} is the relevant photoelastic constant of the quartz crystal, and E_x is the electric field of the optical cavity mode. Similarly, the dominant strain component $S \equiv S_z = \partial u_z/\partial z$, where u_z is the displacement field of the phonon mode. We use the normal mode expansion of the electric and acoustic displacement fields [i.e., $E_x(z) = \sum_j E_j \sin(k_j z)\left(a_j + a_j^{\dagger}\right)$ and $u_z(z) = \sum_m U_m \cos(q_m(z-d))(b_m + b_m^{\dagger})$] to obtain the following interaction Hamiltonian in the rotating wave approximation

$$H^{\mathrm{int}} = -\sum_{j,j',m} \int dV \epsilon_0 \epsilon_r^2 p_{13} q_m U_m E_j E_{j'} \sin(k_j z)\sin(k_{j'} z)\sin(q_m(z-d)) \times \left(a_j^{\dagger} a_{j'} b_m + a_j a_{j'}^{\dagger} b_m^{\dagger}\right) \quad (1)$$

where $E_j = \sqrt{\hbar\omega_j/(\epsilon_0 \epsilon_r V_{\mathrm{opt}})}$ ($U_m = \sqrt{\hbar/(\rho V_{\mathrm{ac}} \Omega_m)}$) is the zero-point amplitude of the electric (acoustic) field, k_j (q_m) is the optical (acoustic) wave vector of the standing-wave optical (acoustic) mode, V_{opt} (V_{ac}) is the effective mode volume of the optical (acoustic) mode, d is the position of the crystal within the optical cavity, and ρ is the mass density of the crystal (see section S2D). Expressing Eq. 1 as $-\sum_m \hbar g_0^m \left(a_j^{\dagger} a_{j'} b_m + a_j a_{j'}^{\dagger} b_m^{\dagger}\right)$, we see that the single-photon coupling rate g_0^m for intermodal optomechanical coupling between two optical modes (ω_j, k_j) and (ω_{j+1}, k_{j+1}) mediated by a phonon mode (Ω_m, q_m) is given by

$$\hbar g_0^m = \int dV \epsilon_0 \epsilon_r^2 p_{13} q_m U_m E_j E_{j'} \sin(k_j z)\sin(k_{j'} z)\sin(q_m(z-d)) \quad (2)$$

Using the parameters of our system, Eq. 2 predicts a maximum single-photon coupling rate of $|g_0^m| \simeq 2\pi \times 24$ Hz. Note that this coupling rate is produced by a phonon mode with a motional mass of 20 μg, which is 1 million to 100 million times larger than previous gigahertz frequency optomechanical systems (see Materials and Methods) (*12*, *13*, *31*).

The wave vector–selective nature of this coupling enables new approaches to precisely tailor interaction with one or more phonon modes. This system differs from conventional Brillouin scattering because even phonon modes that satisfy both energy conservation and

phase-matching requirements can have vanishing optomechanical coupling rates. This intriguing new feature arises because the coupling to a particular phonon mode also depends on the location of the crystal (d) inside the optical cavity. For instance, the overlap integral in Eq. 2 yields a coupling rate of zero when the position of the crystal is such that nodes of a phonon mode coincide with the antinodes of the optical forcing function.

Despite the fact that this current apparatus does not permit us to change the crystal position, we can still control the number of phonon modes that participate in the optomechanical interaction. Independent of crystal location, a pair of adjacent optical modes is guaranteed to couple to at least one phonon mode near the Brillouin frequency because the phase-matching condition is relaxed by the crystal's finite length. However, by using optical resonances at different wavelengths, one can change the position of the nodes inside the crystal, thereby selecting a different group of phonons to mediate optomechanical coupling (see section S2D).

RESULTS

Probing coherent optomechanical response

We explore the optomechanical coupling in our system by probing its coherent response to an optical drive. Specifically, we use the well-known techniques called optomechanically induced amplification (OMIA) and optomechanically induced transparency (OMIT) (*32*).

These measurements are performed using a tunable laser at frequency ω_l, whose output is split into two arms (see Fig. 2A). Laser light in one arm is intensity-modulated at a variable frequency (Ω) using a microwave generator. Light in the other arm is frequency-shifted to $\omega_l + 2\pi \times 44.0$ MHz using an acousto-optic modulator (AOM). This AOM-shifted light acts as a local oscillator (LO) such that the Stokes and anti-Stokes signals appear as distinct tones in the radio-frequency (rf) spectrum analyzer during heterodyne detection. The tones at frequencies ω_l and $\omega_l - \Omega$ serve as control and probe lasers, respectively. The strong control laser (ω_l) drives the higher-frequency optical mode at ω_{j+1}, whereas the weak probe laser ($\omega_p = \omega_l - \Omega$) is swept near the lower-frequency optical mode at ω_j (see inset i of Fig. 2A). The third tone at $\omega_l + \Omega$ is irrelevant, as it is not resonant with the optical cavity modes. Light is delivered to and collected from the optical cavity through a combination of fiber collimators and free-space optics. Light transmitted through the optical cavity is combined with the LO and detected using a photoreceiver, which is connected to an rf spectrum analyzer. This spectrum analyzer monitors the beat note between the transmitted probe laser and the LO by tracking the frequency (Ω) of the microwave generator. Heterodyne detection of the probe light transmitted through the optical cavity provides a direct measurement of the intracavity probe power.

This OMIA measurement (Fig. 2B) reveals a broad optical cavity resonance of linewidth $\kappa_j \simeq 2\pi \times 73$ MHz, consistent with the mirrors' reflectivities. Near the center of the optical resonance, we find three narrow resonances (see inset ii of Fig. 2B) corresponding to phonon modes near the Brillouin frequency of 12.661 GHz. These resonances are equally spaced by ~612 kHz, the expected acoustic FSR $\upsilon_a/2L_{ac}$.This result demonstrates optomechanical coupling to multiple high-frequency longitudinal phonon modes, in a manner consistent with the phase matching described by Eq. 2.

In what follows, we tune the optical wavelength to excite a different pair of optical resonances, ensuring that only a single-phonon mode mediates the optomechanical interaction. A typical OMIA spectrum in which the optomechanical coupling is mediated by a single-phonon mode is shown in Fig. 3A. We perform both OMIA and OMIT measurements to determine the associated single-photon coupling rate and the intrinsic mechanical damping rate. When the system is driven by a strong control laser and a weak probe, we can describe the OMIA (OMIT) phenomena with a linearized interaction Hamiltonian

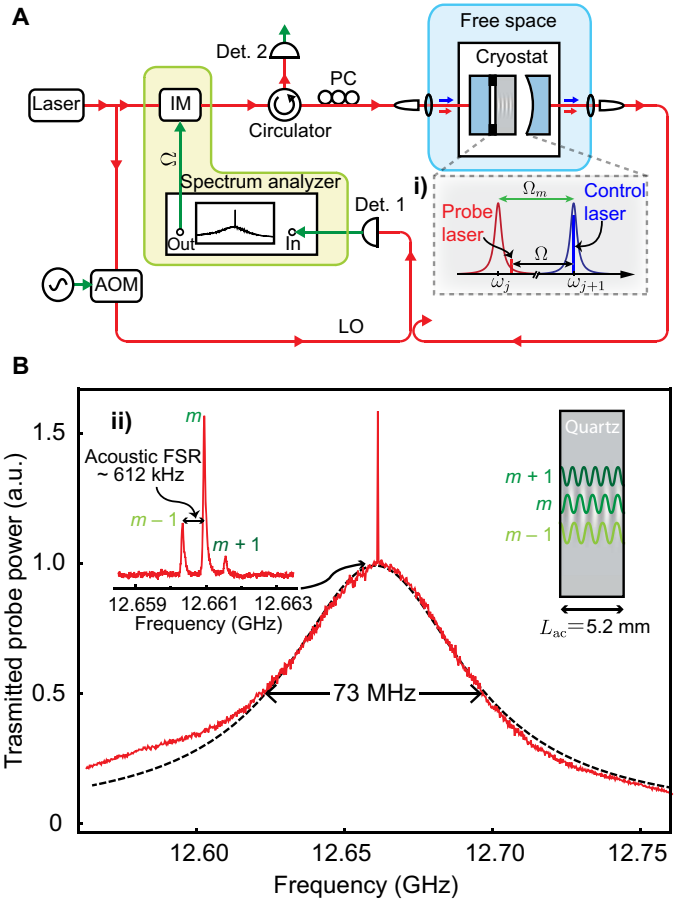

Fig. 2. Optomechanical coupling to a multitude of phonon modes. (**A**) Schematic of the measurement setup used to perform OMIA. A strong control and a weak probe laser are synthesized from the same tunable laser source using an intensity modulator (IM). This light is coupled into and out of the optical cavity using fiber-optic collimators and free-space lenses. The frequency of the tunable laser is set so that the control laser is directly on resonance with the high-frequency optical mode at ω_{j+1} (see inset i). The probe laser is swept near the lower cavity mode at frequency ω_j by sweeping the rf drive frequency (Ω) of the intensity modulator. To examine the coherent response of the intracavity probe field due to optomechanical coupling, a heterodyne measurement is performed between the transmitted probe light and the AOM-shifted laser light. (**B**) We observe coherent buildup of the intracavity photon number as the probe laser is scanned near the optical mode ω_j. The optical cavity decay rate of $\kappa_j \simeq 2\pi \times 73$ MHz obtained for this mode is consistent with the losses at the two mirrors. In addition, we see sharp resonances on the optical mode spectrum corresponding to the phonon-mediated transfer of energy from the high-frequency optical mode at frequency ω_{j+1} to the lower-frequency optical mode at ω_j. A close zoom in of the optical mode spectrum near the center of the optical resonance reveals three high-frequency acoustic modes around 12.661 GHz with a frequency spacing of ~612 kHz (see inset ii). This frequency spacing is consistent with the acoustic FSR of $\upsilon_a/2L_{ac}$ for the standing-wave longitudinal modes formed in crystalline quartz along the z axis. These acoustic modes have very high longitudinal mode numbers (or overtone number) of $m \approx 2.08 \times 10^4$.

$H_{\rm int}^m = -\hbar g_0^m \sqrt{n_c}\left(a_j b_m + a_j^\dagger b_m^\dagger\right)$ $\left(H_{\rm int}^m = -\hbar g_0^m \sqrt{n_c}\left(a_{j+1}^\dagger b_m + b_m^\dagger a_{j+1}\right)\right)$, where n_c is the intracavity photon number for the optical mode at ω_{j+1} (ω_j). Assuming that the control laser is directly on resonance with the optical mode at ω_{j+1} (ω_j), this effective Hamiltonian predicts a relative OMIA peak height (OMIT dip) of $1/(1 \mp C)^2$, when $\Omega = \Omega_m$. Here, $C = 4n_c|g_0^m|^2/(\kappa\Gamma_m)$ is the cooperativity and Γ_m is the intrinsic mechanical damping rate. Moreover, the linewidth of this OMIA peak (OMIT dip) is given by $\Gamma_{\rm eff} = (1 \mp C)\Gamma_m$ (*15*).

To measure Γ_m and g_0^m, we varied the control laser power and measured the relative heights and linewidths of the OMIA peaks (OMIT dips) (see Fig. 3, B to G). As expected from theory, the relative heights of the OMIA peaks (OMIT dips) increased (decreased) nonlinearly, whereas the effective linewidth, $\Gamma_{\rm eff}$, decreased (increased) linearly as the control laser power was increased from 7.8 to 118 mW. Extrapolating the linear fit in Fig. 3G to zero input power gives $\Gamma_m \simeq 2\pi \times 86$ kHz (acoustic Q factor $\simeq 1.5 \times 10^5$). To understand the acoustic linewidth characteristics, it is useful to view the acoustic propagation within the quartz crystal as being analogous to optical beam propagation within a Fabry-Pérot cavity. This is because the acoustic wavelength (~500 nm) is much smaller than the lateral extent

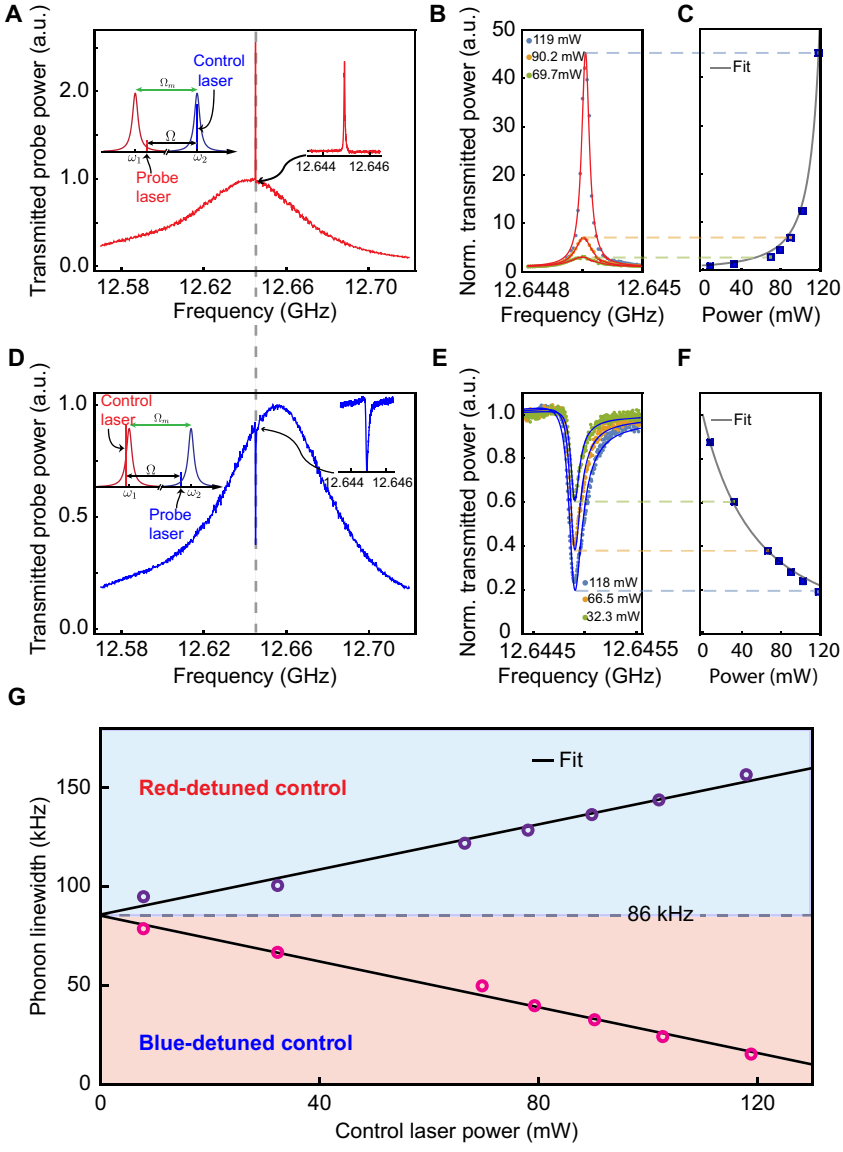

Fig. 3. Characterization of the zero-point coupling rate and the mechanical dissipation rate. (**A**) We perform OMIA measurements on a single-phonon mode using a blue-detuned control laser that is resonant with the high-frequency optical mode (see inset). (**B**) As we increase the power in the control laser, the height of the peak corresponding to the OMIA signal increases nonlinearly with the control laser power, as displayed in (**C**). The linewidth of the OMIA peak, however, decreases with the control power, as seen in (**G**). (**D**) OMIT measurements are performed with the same phonon mode by simply red-detuning the control laser. Note that, because the control laser has a slight offset relative to the low-frequency optical mode at ω_j, the center of the cavity resonance shifts, but the OMIT dip is observed exactly at a phonon frequency of 12.645 GHz. (**E**) The dip of the OMIT signal decreases nonlinearly as a function of the control power, as displayed in (**F**). The linewidth of the OMIT signal, however, increases linearly with the control power, as seen in (G). From the dependence of linewidth as a function of the control laser power, we obtain a cold cavity linewidth $\Gamma_m/2\pi \simeq 86$ kHz for the phonon mode at 12.645 GHz.

of the excited acoustic mode (beam radius ≃ 43 μm) within the crystal. Analogous to diffraction losses within an optical Fabry-Pérot cavity, propagation of a Gaussian acoustic beam within the planar quartz crystal introduces acoustic diffraction losses, which is the dominant source of loss in this present system (see section S5). However, these acoustic Q factors can be markedly increased by shaping the surfaces of the quartz crystal to compensate for the effects of diffraction (*24*).

The cooperativities (C) and intrinsic mechanical damping rate (Γ_m) obtained from experiments along with n_c calculated from measuring input control laser power P_{in} give $g_0^m \approx 2\pi \times 18$ Hz, consistent with the theoretically predicted maximum value of $2\pi \times 24$ Hz (see sections S2 and S3). Note that, based on the measured normalized reflection spectrum (see Fig. 1D) and fraction of light transmitted (85%) on resonance, we assumed critical coupling to the optical mode and negligible internal losses (i.e., $\kappa_i \ll 2\kappa^{\text{ext}}$) while calculating n_c from P_{in}. So far, we have probed the system's coherent response. Next, we explore thermal fluctuations of the phonon mode and self-sustained oscillations (*15*) as we increase the cooperativity to greater than unity.

Thermal fluctuations and phonon self-oscillation

We measure thermal fluctuations of the mechanical mode through spontaneous light-scattering measurements. We use a control laser that is resonant with the higher-frequency optical mode ω_{j+1} (see Fig. 4A); no probe field is supplied for these measurements. The thermally populated phonon mode mediates scattering of incident control photons from frequency ω_{j+1} to ω_j through the Stokes process. Heterodyne detection is used to monitor the power spectrum of this spontaneously scattered Stokes light, as shown in the inset i of Fig. 4B. As the control laser power is increased, we observe a sharp increase in the magnitude of the scattered Stokes light accompanied by spectral narrowing of the heterodyne beat tone (inset ii of Fig. 4B). Optomechanical systems in the blue-detuned regime display these lasing transitions at $C = 1$, when $\Gamma_{\text{eff}} = \Gamma_m(1 - C) = 0$. When $\Gamma_{\text{eff}} < 0$ (i.e., $C > 1$), parametric instability initially causes thermal fluctuations to grow exponentially in time and eventually saturate to reach coherent self-sustained oscillations. This phenomenon is well studied in many optomechanical systems (*29*, *33*) and is also commonly known as "phonon lasing" (*15*). The measurement of total backscattered light from the cavity using a power meter as a function of the input control laser power (Fig. 4B) reveals a self-oscillation threshold of 137 mW, consistent with the threshold (~140 mW) predicted from the measured values of n_c, g_0^m, κ, and Γ_m. The total output Stokes power after lasing is consistent with a slope efficiency of 62% (see section S6A). Note that the intracavity photon number $n_c \approx 6.3 \times 10^9$ is achieved for the highest available control laser power of 204 mW. Such a large intracavity photon number produces cavity-enhanced coupling rate of $g_m = \sqrt{n_c} g_0^m = 2\pi \times 1.5$ MHz and $C = 1.4$. This coupling rate is already more than 10 times larger than Γ_m, as required for high-fidelity transduction of quantum information from the optical to the mechanical domain (or vice versa) (*27*). Last, we note that, although the low signal-to-noise ratio prevented us from measuring thermal fluctuations using a red-detuned drive, these measurements can be readily performed by improving the finesse of the optical cavity (*34*).

DISCUSSION

These results lay the foundation for a promising new class of macroscopic cavity optomechanical systems that rely on bulk acoustic modes of a crystalline solid—rather than subwavelength structural control—to achieve high-frequency multimode interactions. Because phase matching determines the phonon frequency, this approach permits coupling to massive (20 μg), high-frequency phonon modes without size reduction. Resonant optical driving of this multimode system produces appreciable coupling rates (1.5 MHz) to high-frequency (13 GHz) phonons and $C > 1$. These results are obtained using the simplest of flat-flat crystal geometries, meaning that these same principles can be readily used to transform practically any transparent crystal into a high-frequency cavity optomechanical system. Because the Brillouin frequency depends on the optical wavelength and material parameters, these same strategies can be used to harness phonons over a tremendous range of frequencies (e.g., 5 to 100 GHz) by designing the system around different wavelengths and materials. The versatility and robustness of this strategy should lend itself to new types of hybrid

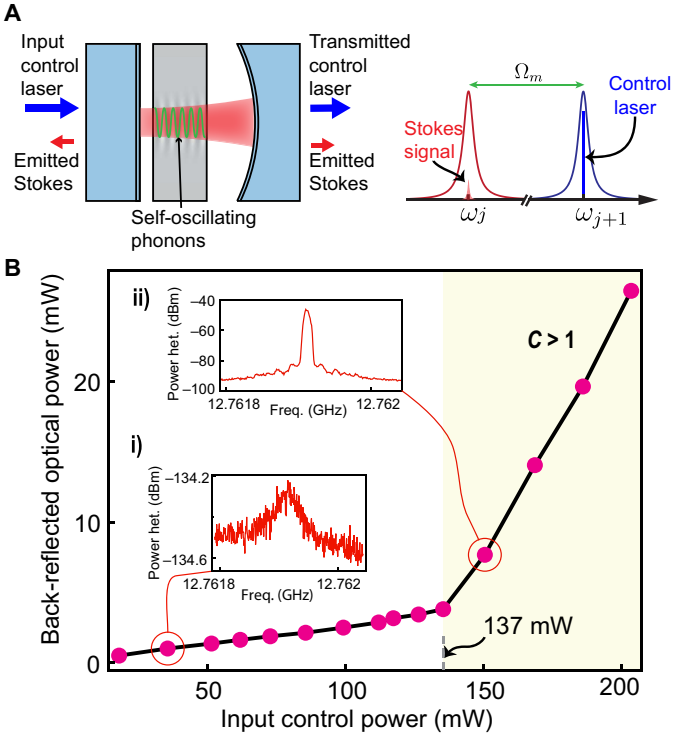

Fig. 4. Thermal fluctuations and regenerative self-oscillations of a high-frequency phonon mode. (**A**) To observe thermal fluctuations of the phonon mode, we turn off the probe laser and tune a strong control laser directly on resonance with the high-frequency optical mode. The thermally populated phonon mode spontaneously scatters light from the higher-energy optical mode to the lower-energy optical mode (Stokes field); this light exits our optical system through both mirrors. (**B**) From the measurement of back-reflected optical power as a function of the input control laser power, we observe a clear threshold behavior at 137 mW corresponding to regenerative self-oscillation of the phonon mode (i.e., $C = 1$). Before threshold, a small (~2.6%) back-reflection results from imperfect coupling of the control laser to the optical mode at ω_2. However, once self-oscillating, phonons scatter a large fraction of the input control laser into the Stokes light, which exits the optical cavity through both forward and backward directions, a substantial increase in the back-reflected optical power occurs. Furthermore, from the heterodyne beat tone of the scattered Stokes light with the frequency-shifted version of the input control laser, we observe a dramatic line narrowing of phonons as we cross the lasing threshold, as displayed in insets i and ii.

quantum systems, new forms of materials spectroscopy, and studies of laser-oscillator physics.

Our quartz-based optomechanical system has many promising features in the context of cavity quantum optomechanics. Large optomechanical coupling rates (>60 MHz) to these high-frequency phonons could be achieved even without miniaturization because this macroscopic system can store a large number of intracavity photons ($>10^{13}$) through resonant driving (*35*). The demonstrated coupling rate of 1.5 MHz is already large enough to enter the strong-coupling regime ($g_m > \kappa/2, \Gamma_m/2$) if the optical finesse is boosted from its current value ($\mathcal{F} \approx 170$) to $\mathcal{F} \approx 10^4$. In this regime, one can deterministically swap excitations between the optical and phononic domains for quantum transduction and the creation of nonclassical mechanical states (*15*). Moreover, because of the potential for reduced thermal decoherence and the opportunity to reach phonon counting sensitivities of less than one, this system shows great promise as a platform to implement probabilistic schemes for quantum-state preparation (see section S8). Owing to the low (high) optical absorption (thermal conductivity) of pristine crystalline quartz [<4.3 dB/km (*36*)] and greatly reduced ($<10^{-4}$) photon-surface interactions relative to high-frequency microscale counterparts (*12*), this system offers a promising path to robust quantum optomechanics.

Hybrid quantum systems using long-lived phonons within bulk acoustic resonators could be a valuable resource for quantum information processing. It is possible to increase the Q factor of these high-frequency phonons within quartz from their present values (1.5×10^5) to 4×10^7 by shaping the acoustic resonator into a plano-convex geometry (*24*). These highly coherent bulk acoustic modes could then be useful as quantum memories. Moreover, these high-Q phonon modes could readily permit strong coupling to individual defect centers for quantum information processing (see section S5), a result that is perhaps surprising given the large acoustic mode volumes relative to previous proposals (*37*, *38*). Simultaneous optomechanical and electromechanical control of bulk acoustic wave phonons within piezoelectric crystals also offers a path toward high-fidelity microwave-to-optical conversion (*39*, *40*).

Beyond the conventional goals of quantum optomechanics, this optomechanical system presents new opportunities for materials spectroscopy and precision measurement. Sensitive metrology of cryogenic phonon physics and defect centers can be performed in a wide array of materials to understand various decoherence channels for phonons. Moreover, bulk acoustic resonators show great potential for quantum noise–limited optomechanical oscillators with ultranarrow fundamental linewidth (<1 nHz) as they can support large coherent phonon populations ($>10^{12}$) (see section S6). These highly coherent oscillators could be used for precision sensing (*41*), time keeping (*42*), and the exploration of new physics (*43*).

MATERIALS AND METHODS

The planar crystalline z-cut α-quartz crystal (Aa grade) used for this experiment was obtained commercially from Rocky Mountain Instrument Co. For the theoretical estimate of the coupling rate, we used the following parameters: $n = 1.55$, $p_{13} = 0.27$, $\rho = 2648\ \mathrm{kg/m^3}$, $L_{\mathrm{opt}} = 9.13$ mm, $L_{\mathrm{ac}} = 5.19$ mm, $A \simeq \pi \times (61\ \mu\mathrm{m})^2$, $\omega_j = 2\pi \times 193.4$ THz, and $\Omega_m = 2\pi \times 12.65$ GHz (see section S2D).

The Gaussian optical modes, with beam waist $w_{\mathrm{opt}} \simeq 61\ \mu$m, drive a longitudinal standing-wave phonon mode with Gaussian transverse profile with beam waist $w_{\mathrm{ac}} \simeq 43\ \mu$m. Therefore, the effective motional mass of the phonon mode in our system $m_{\mathrm{eff}} \approx \pi\rho L_{\mathrm{ac}} w_{\mathrm{ac}}^2/4 = 20\ \mu$g.

SUPPLEMENTARY MATERIALS

Supplementary material for this article is available at http://advances.sciencemag.org/cgi/content/full/5/4/eaav0582/DC1

REFERENCES AND NOTES

1. J. I. Cirac, P. Zoller, Quantum computations with cold trapped ions. *Phys. Rev. Lett.* **74**, 4091–4094 (1995).
2. A. D. O'Connell, M. Hofheinz, M. Ansmann, R. C. Bialczak, M. Lenander, E. Lucero, M. Neeley, D. Sank, H. Wang, M. Weides, J. Wenner, J. M. Martinis, A. N. Cleland, Quantum ground state and single-phonon control of a mechanical resonator. *Nature* **464**, 697–703 (2010).
3. J. Teufel, D. Li, M. Allman, K. Cicak, A. Sirois, J. Whittaker, R. Simmonds, Circuit cavity electromechanics in the strong-coupling regime. *Nature* **471**, 204–208 (2011).
4. Y. Chu, P. Kharel, W. H. Renninger, L. D. Burkhart, L. Frunzio, P. T. Rakich, R. J. Schoelkopf, Quantum acoustics with superconducting qubits. *Science* **358**, 199–202 (2017).
5. T. Stowe, K. Yasumura, T. Kenny, D. Botkin, K. Wago, D. Rugar, Attonewton force detection using ultrathin silicon cantilevers. *Appl. Phys. Lett.* **71**, 288–290 (1997).
6. K. Stannigel, P. Rabl, A. S. Sørensen, P. Zoller, M. D. Lukin, Optomechanical transducers for long-distance quantum communication. *Phys. Rev. Lett.* **105**, 220501 (2010).
7. K. C. Lee, B. J. Sussman, M. R. Sprague, P. Michelberger, K. F. Reim, J. Nunn, N. K. Langford, P. J. Bustard, D. Jaksch, I. A. Walmsley, Macroscopic non-classical states and terahertz quantum processing in room-temperature diamond. *Nat. Photonics* **6**, 41–44 (2012).
8. C. H. Metzger, K. Karrai, Cavity cooling of a microlever. *Nature* **432**, 1002–1005 (2004).
9. A. Schliesser, P. Del'Haye, N. Nooshi, K. Vahala, T. Kippenberg, Radiation pressure cooling of a micromechanical oscillator using dynamical backaction. *Phys. Rev. Lett.* **97**, 243905 (2006).
10. F. Brennecke, S. Ritter, T. Donner, T. Esslinger, Cavity optomechanics with a Bose-Einstein condensate. *Science* **322**, 235–238 (2008).
11. J. D. Thompson, B. M. Zwickl, A. M. Jayich, F. Marquardt, S. M. Girvin, J. G. E. Harris, Strong dispersive coupling of a high-finesse cavity to a micromechanical membrane. *Nature* **452**, 72–75 (2008).
12. M. Eichenfield, J. Chan, R. M. Camacho, K. J. Vahala, O. Painter, Optomechanical crystals. *Nature* **462**, 78–82 (2009).
13. L. Ding, C. Baker, P. Senellart, A. Lemaitre, S. Ducci, G. Leo, I. Favero, High frequency GaAs nano-optomechanical disk resonator. *Phys. Rev. Lett.* **105**, 263903 (2010).
14. G. Bahl, M. Tomes, F. Marquardt, T. Carmon, Observation of spontaneous Brillouin cooling. *Nat. Phys.* **8**, 203–207 (2012).
15. M. Aspelmeyer, T. J. Kippenberg, F. Marquardt, Cavity optomechanics. *Rev. Mod. Phys.* **86**, 1391–1452 (2014).
16. J. Chan, T. M. Alegre, A. H. Safavi-Naeini, J. T. Hill, A. Krause, S. Gröblacher, M. Aspelmeyer, O. Painter, Laser cooling of a nanomechanical oscillator into its quantum ground state. *Nature* **478**, 89–92 (2011).
17. J. D. Cohen, S. M. Meenehan, G. S. MacCabe, S. Gröblacher, A. H. Safavi-Naeini, F. Marsili, M. D. Shaw, O. Painter, Phonon counting and intensity interferometry of a nanomechanical resonator. *Nature* **520**, 522–525 (2015).
18. S. Hong, R. Riedinger, I. Marinković, A. Wallucks, S. G. Hofer, R. A. Norte, M. Aspelmeyer, S. Gröblacher, Hanbury Brown and Twiss interferometry of single phonons from an optomechanical resonator. *Science* **358**, 203–206 (2017).
19. K. C. Lee, M. R. Sprague, B. J. Sussman, J. Nunn, N. K. Langford, X.-M. Jin, T. Champion, P. Michelberger, K. F. Reim, D. England, D. Jaksch, I. A. Walmsley, Entangling macroscopic diamonds at room temperature. *Science* **334**, 1253–1256 (2011).

20. R. Riedinger, A. Wallucks, I. Marinković, C. Löschnauer, M. Aspelmeyer, S. Hong, S. Gröblacher, Remote quantum entanglement between two micromechanical oscillators. *Nature* **556**, 473–477 (2018).
21. C. Ockeloen-Korppi, E. Damskägg, J.-M. Pirkkalainen, M. Asjad, A. Clerk, F. Massel, M. Woolley, M. Sillanpää, Stabilized entanglement of massive mechanical oscillators. *Nature* **556**, 478–482 (2018).
22. O. Arcizet, R. Rivière, A. Schliesser, G. Anetsberger, T. J. Kippenberg, Cryogenic properties of optomechanical silica microcavities. *Phys. Rev. A* **80**, 021803 (2009).
23. S. Galliou, M. Goryachev, R. Bourquin, P. Abbé, J. P. Aubry, M. E. Tobar, Extremely low loss phonon-trapping cryogenic acoustic cavities for future physical experiments. *Sci. Rep.* **3**, 2132 (2013).
24. W. H. Renninger, P. Kharel, R. O. Behunin, P. T. Rakich, Bulk crystalline optomechanics. *Nat. Phys.* **14**, 601–607 (2018).
25. P. Kharel, Y. Chu, M. Power, W. H. Renninger, R. J. Schoelkopf, P. T. Rakich, Ultra-high-Q phononic resonators on-chip at cryogenic temperatures. *APL Photonics* **3**, 066101 (2018).
26. M. R. Vanner, M. S. Aspelmeyer, M. Kim, Quantum state orthogonalization and a toolset for quantum optomechanical phonon control. *Phys. Rev. Lett.* **110**, 010504 (2013).
27. A. S. Parkins, H. J. Kimble, Quantum state transfer between motion and light. *J. Opt. B Quantum Semiclass. Opt.* **1**, 496–504 (1999).
28. M. J. Woolley, A. A. Clerk, Two-mode squeezed states in cavity optomechanics via engineering of a single reservoir. *Phys. Rev. A* **89**, 063805 (2014).
29. G. Anetsberger, E. M. Weig, J. P. Kotthaus, T. J. Kippenberg, Cavity optomechanics and cooling nanomechanical oscillators using microresonator enhanced evanescent near-field coupling. *C. R. Phys.* **12**, 800–816 (2011).
30. K. Børkje, S. Girvin, Quantum optomechanics with a high-frequency dilational mode in thin dielectric membranes. *New J. Phys.* **14**, 085016 (2012).
31. M. Mitchell, B. Khanaliloo, D. P. Lake, T. Masuda, J. Hadden, P. E. Barclay, Single-crystal diamond low-dissipation cavity optomechanics. *Optica* **3**, 963–970 (2016).
32. S. Weis, R. Rivière, S. Deléglise, E. Gavartin, O. Arcizet, A. Schliesser, T. J. Kippenberg, Optomechanically induced transparency. *Science* **330**, 1520–1523 (2010).
33. I. S. Grudinin, H. Lee, O. Painter, K. J. Vahala, Phonon laser action in a tunable two-level system. *Phys. Rev. Lett.* **104**, 083901 (2010).
34. P. Kharel, Y. Chu, E. A. Kittlaus, N. T. Otterstrom, S. Gertler, P. T. Rakich, Multimode strong coupling in cavity optomechanics. arXiv:1812.06202 [physics.optics] (14 December 2018).
35. L. S. Meng, J. K. Brasseur, D. K. Neumann, Damage threshold and surface distortion measurement for high-reflectance, low-loss mirrors to 100+ MW/cm^2 cw laser intensity. *Opt. Express* **13**, 10085–10091 (2005).
36. D. Pinnow, T. Rich, Development of a calorimetric method for making precision optical absorption measurements. *Appl. Opt.* **12**, 984–992 (1973).
37. Ö. O. Soykal, R. Ruskov, C. Tahan, Sound-based analogue of cavity quantum electrodynamics in silicon. *Phys. Rev. Lett.* **107**, 235502 (2011).
38. T. Ramos, V. Sudhir, K. Stannigel, P. Zoller, T. J. Kippenberg, Nonlinear quantum optomechanics via individual intrinsic two-level defects. *Phys. Rev. Lett.* **110**, 193602 (2013).
39. J. Bochmann, A. Vainsencher, D. D. Awschalom, A. N. Cleland, Nanomechanical coupling between microwave and optical photons. *Nat. Phys.* **9**, 712–716 (2013).
40. R. W. Andrews, R. W. Peterson, T. P. Purdy, K. Cicak, R. W. Simmonds, C. A. Regal, K. W. Lehnert, Bidirectional and efficient conversion between microwave and optical light. *Nat. Phys.* **10**, 321–326 (2014).
41. K. Jensen, K. Kim, A. Zettl, An atomic-resolution nanomechanical mass sensor. *Nat. Nanotechnol.* **3**, 533–537 (2008).
42. M. E. Tobar, J. G. Hartnett, E. N. Ivanov, D. Cros, P. Blondy, P. Guillon, Cryogenically cooled sapphire-rutile dielectric resonators for ultrahigh-frequency stable oscillators for terrestrial and space applications [atomic frequency standards]. *IEEE Trans. Microw. Theory Tech.* **48**, 1265–1269 (2000).
43. P. Wolf, S. Bize, A. Clairon, A. N. Luiten, G. Santarelli, M. E. Tobar, Tests of Lorentz invariance using a microwave resonator. *Phys. Rev. Lett.* **90**, 060402 (2003).
44. P. T. Rakich, P. Davids, Z. Wang, Tailoring optical forces in waveguides through radiation pressure and electrostrictive forces. *Opt. Express* **18**, 14439–14453 (2010).
45. C. H. Dong, Z. Shen, C. L. Zou, Y. L. Zhang, W. Fu, G. C. Guo, Brillouin-scattering-induced transparency and non-reciprocal light storage. *Nat. Commun.* **6**, 6193 (2015).
46. W. R. Leeb, Losses introduced by tilting intracavity etalons. *Appl. Phys.* **6**, 267–272 (1975).
47. B. L. Green, S. Mottishaw, B. G. Breeze, A. M. Edmonds, U. F. S. D'Haenens-Johansson, M. W. Doherty, S. D. Williams, D. J. Twitchen, M. E. Newton, Neutral silicon-vacancy center in diamond: Spin polarization and lifetimes. *Phys. Rev. Lett.* **119**, 096402 (2017).
48. N. T. Otterstrom, R. O. Behunin, E. A. Kittlaus, Z. Wang, P. T. Rakich, A silicon Brillouin Laser. *Science* **360**, 1113–1116 (2018).
49. K. J. Vahala, Back-action limit of linewidth in an optomechanical oscillator. *Phys. Rev. A* **78**, 023832 (2008).

Acknowledgments: We thank Y. Chu, V. Jain, S. Gertler, T. Yoon, C. Brown, Y. Zhou, and Y. Luo for helpful discussions and feedback. **Funding:** We acknowledge funding support from ONR YIP (N00014-17-1-2514), NSF MRSEC (DMR-1119826), AFOSR (FA9550-09-1-0484 and FA9550-15-1-0270), ONR MURI on Quantum Optomechanics (award no. N00014-15-1-2761), and the Packard Fellowship for Science and Engineering. N.T.O. acknowledges support from the NSF Graduate Research Fellowship under grant no. DGE1122492. **Author contributions:** P.K., G.I.H., and E.A.K. performed the experiments, and P.K. analyzed the data with input from J.G.E.H. and P.T.R. P.K. developed the analytical theory with guidance from G.I.H., J.G.E.H., and P.T.R. W.H.R. contributed to the models of photon-phonon coupling, and N.T.O. aided in the development of experimental techniques. All authors participated in the writing of this manuscript. **Competing interests:** The authors declare that they have no competing interests. **Data and materials availability:** All data needed to evaluate the conclusions in the paper are present in the paper and/or the Supplementary Materials. Additional data related to this paper may be requested from the authors.

Submitted 9 August 2018
Accepted 13 February 2019
Published 5 April 2019
10.1126/sciadv.aav0582

Citation: P. Kharel, G. I. Harris, E. A. Kittlaus, W. H. Renninger, N. T. Otterstrom, J. G. E. Harris, P. T. Rakich, High-frequency cavity optomechanics using bulk acoustic phonons. *Sci. Adv.* **5**, eaav0582 (2019).